Ray tracing study of ITER in-vessel lighting system

Shin Kajita,[1, a)] Gilles Passedat,[2] and Roger Reichle[3]
[1)] *Institute of Materials and Systems for Sustainability, Nagoya University, Nagoya 464-8603, Japan*
[2)] *CLAVIS S.A.R.L., 29 Boulevard Marius Thomas 13007 Marseille 7, France*
[3)] *ITER organization, Route de Vinon-sur-Verdon, CS 90 046, 13067 St. Paul Lez Durance Cedex, France*

(Dated: 18 March 2020)

In-vessel lighting system is being developed for ITER. The diagnostic system is for inspecting and detecting eventual damages and defects of in-vessel components between discharges by illuminating the vacuum vessel with light sources. In this work, feasibility study of the in-vessel lighting system is performed using a ray tracing simulation. We installed sources and detectors in a ray tracing model using the field of views of wide-angle viewing systems and calculated the radiance profiles at detectors for different wall reflection scenarios. It was found that the wall is uniformly illuminated when the wall has a diffuse reflectance while the specular case has more brightness. We will discuss feasibility of the diagnostics system based on expected signal and noise levels.

I. INTRODUCTION

Inspection of vacuum vessel is important to keep the safety and the quality of the plasma performance in ITER. It is necessary to see various locations of the vacuum vessel while illuminating them properly. It is inevitable to check the condition of the vacuum vessel between pulses in a limited amount of time. Because accessibility of ITER is much more limited than present experimental fusion devices, it should be designed properly before all the diagnostics systems were installed.

There are various options for light sources to illuminate inside the vessel. For example, installations of tungsten lamps, tungsten filaments, and laser beams are the candidates. The tungsten lamps and tungsten filaments may be installed in the port plug or interspace (between the port plug and port cell), and the laser require dedicated laser paths. Considering the space allocation, risks, and feasibility, one of the best solutions is to illuminate the vessel and record images with using the optics and cameras of exploitable infrared (IR) and visible wide angle viewing systems (WAVS)[1–3].

In this study, we assess the feasibility of above scenario by conducting ray tracing simulations. In the next section, we briefly explain the design and models for the ray tracing simulation. Then, in Sec. III, we show results of ray tracing simulation on various cases with different optical properties. Based on the calculation results, we will discuss the feasibility of the illuminating systems in Sec. IV. Necessary integration time and a way to shorten the total integration time will be shown.

II. ILLUMINATION SYSTEM

A. Design

In this system, the light will be transferred through optical fibers from lasers located in the diagnostic building to optical heads located behind the bioshield. The optical head has

[a)] Electronic mail: kajita.shin@nagoya-u.jp

two positions: a parked position and a working position. In the working position, the fiber can inject the light in the WAVS optical path in the reverse direction so that the light can go through the aperture and illuminate the vessel.

In order to achieve the maximum beam divergence at the aperture output, it is necessary to increase the natural laser head etendue and adapt it to the etendue of the WAVS optical path. One of the best lasers for this option is 793 nm fibered laser diodes, which enable to produce a high-power beam at a reduced cost. The wavelength allows visible cameras to take images with a good spatial resolution. In this configuration, because the recording path cannot be used for illumination, recording for different field of views will be basically sequential.

Figure 1 shows a schematic of a bird's eye view of ITER. Red star markers correspond to the port used for 55.GA (Upper port Visible and Infrared WAVS) and green hexagons represents the ports used for 55.G1 (Equatorial port Visible and Infrared WAVS). 55.GA diagnostics have almost identical five field of views in upper ports (♯2, 8, 11, 14, and 17), and 55.G1 diagnostics have four almost identical systems. Three of them at ♯3, 9, and 17 have four FOVs and the one at ♯12 has three FOVs. The number of the FOV is five for 55.GA and 15 for 55.G1; in total there are 20 FOVs.

B. Ray tracing model

We use a three-dimensional model of the ITER full vacuum vessel which was developed in Ref. 4. The commercial simulation software LightTools was used for ray tracing. To run simulations, it is necessary to install receivers (detector) and light sources.

Figure 2(a) shows a computer aided design diagram of one of the 55.G1 system including FOVs. There are three (in ♯12) or four (in ♯3, 9, and 17) FOVs, which observe different directions. The ♯12 has three FOVs observing right, left, and lower directions. Schematics in Fig. 2(b,c) represent the configurations of the receiver and the source. We use a pinhole camera configuration in this study as omitting actual optics for WAVS for simplicity. The receiver was positioned behind the pinhole, and rays will be traced backward from the receiver to sources. Here, aperture was 1 mm in radius which was chosen to be smaller than the actual aperture to obtain a clear image. Ideally, a source is to be allocated behind the pinhole; because the aperture is so small that enough rays cannot be obtained in a realistic time scale. Therefore, we decided to allocate sources inside the vacuum vessel with the same size of the receiver for G1 sources and roughly one order of magnitude greater sources for GA sources. The angle of aperture of the sources was determined based on the field of views of 55.G1 and 55.GA. For simplicity, square shaped target areas were used for the ray tracing, because an installation of oblong apertures was not so simple in the LightTools. As shown later, the size of the bright spot directly from sources will be greater than the actual size. However, because we chose the same angle of aperture, the ray paths did not change so much after reflection at walls. Considering the fact that we eliminated images with direct illumination, one can say that the results are valid for later assessments of radiance and signal levels. Although we omitted the optics of the WAVS for simplicity as using a pinhole camera configuration, the field of views were consistent with those of WAVS. Although the influence of aberrations cannot be included, the pinhole camera configuration will be enough to assess the radiance of the field of view. It is noted that the radiance in photon/s/m^2/sr can be calculated from the obtained illuminance in W/mm^2 considering the size of the pinhole (1 mm in radius), and the distance and angle from the receiver to the pinhole. In this study, we call the positions of the source or detector with the diagnostics name (GA or G1), the port number (♯3 etc.), and letters U, R, L, or D, which means up, right, left, or down directions of FOVs, respectively, namely, for example, GA♯2 and G1♯3U.

Reflectance property of the wall is one of the most important properties that we have to choose carefully for ray tracing calculations. As following previous studies[5], we used a mixture of specular and diffuse reflectance, R_s and R_s, respectively, and change the ratio of those two components, R_d/R_s, while fixing the total reflectance at 50%. Concerning the

specular reflectance, a Gaussian angular profile with 1/e angle of 6 degree is used.

The radiance of the field of views can be obtained considering the size of the pinhole (aperture) and distance between the receiver and the pinhole. The radiance can be determined independent of the receiver configuration. When considering the signal to noise ratio (SNR), it is necessary to consider the optics transmission, the actual aperture size, the detector size, and so on. The details of the SNR analysis will be described in Sec. IV.

III. RAY TRACING

A. Selection of sources

Figure 3(a) shows the radiance profiles at the receiver GA♯2 assuming that the power of the light sources is 1 W. From now on, we always turn off the sources of their own FOV (here, GA♯2 source), because it is difficult to use the source for their own path. Here, R_d/R_s was assumed to be 5/95. A curved dark region corresponds to the divertor tiles, while a left bright area shows a part of blanket modules. In Fig. 3(a), the image was produced by summing up 19 images shown in Fig. 3(b-t), where each one of 19 sources is turned on, respectively, from (b) the source GA♯8 to (t) G1♯17D. Images are very dark (less than 10^{14} ph/s/m^2/sr) except for 6-7 images, indicating that the image shown in Fig. 3(a) can be composed of mainly those 6-7 images such as the ones shown in Fig. 3(h,i,j,l,m,o,s).

Figure 4(a) shows the radiance profiles at the receiver G1♯3R with all the sources turned on except for G1♯3R and G1♯9L sources. Figure 4(b-t) shows radiance profiles on G1♯3R receiver from each one of the 19 sources, respectively. In Fig. 4(i), which corresponds to the illumination from G1♯9L source, very intense square region can be seen around the center. This corresponds to the source directly illuminating the receiver and formed a bright spot. It is necessary to turn off those sources to eliminate saturation of the detector; in Fig. 4(a), G1♯9L source is turned off. In Fig. 4(a), the intensity is strong in the central region mainly because of source G1♯9L, while upper and lower parts are rather dark. Major contributions to this FOV are left-facing sources, i.e. G1♯9L, G1♯12L, G1♯17L, and G1♯3L. Because the FOV faces right direction, left-facing sources contributed more than the others. Similar to the case GA♯2, shown in Fig. 3, more than half of the images were very dark.

Table I summarizes the sources formed a bright spot, the main sources contributing to the total radiance profile, and their fractions for each one of the 20 sources. Bright spots were identified on all the sources faced right or left on ports ♯3, 9, 12, and 17. Those bright spot sources are eliminated when making total radiance profiles for the corresponding receivers. The contribution of the major sources is in the range from 22 to 68%. It is seen from Table I that main contributions for right and left-facing receivers are always left and right-facing sources, respectively.

Figure 5(a) shows the averaged radiance on the 20 receivers. The radiance ranges are 0.1-3$\times 10^{16}$ ph/s/m^2/sr. The radiance on GA receivers was less than 0.5$\times$ 10^{16} ph/s/m^2/sr. Concerning G1 receivers, right and left-facing receivers have higher radiance, i.e. $>$1.5$\times$ 10^{16} ph/s/m^2/sr, compared to those of upward and downward receivers. This was probably because the right-facing and left-facing receivers received intense light from left-facing and right facing sources, respectively.

Figure 5(b) shows the fraction of the contributions from the major sources. The fractions from the first, second, third, fourth, fifth to tenth, and remained sources are separately shown with different bars. The contribution of the first major source was in the range of 22-68%, as shown in Table I. In particular, it is seen that upward sources have lower fraction from the first major source. For all the sources including the upward ones, more than 50% of the total radiance was from the major four sources. When including from the first to the tenth major sources, the fraction will be greater than $\approx$90%.

B. Reflectance property dependence

In the last section, R_d/R_s was assumed to be 5/95, which corresponds to a specular case. Before the surface is exposed to plasmas, the specular component will be dominant, as was shown previously[6]. Bidirectional reflectance distribution function (BRDF) of the tungsten wall material was explained well at $R_d/R_s \approx 98/2$ with two Gaussian components for specular reflectance (major 5 degree and minor 16 degree components)[6]. However, it is likely that the BRDF alters during the discharges by deposition and/or sputtering, and the diffuse component may increase. Figure 6 shows the radiance profiles of typical four receivers ((a-d)GA♯17, (e-h)G1♯17U, (i-l)G1♯17R, and (m-p) G1♯17D) at different R_d/R_s from 5/95 (the rightmost four images) to 25/75 (the leftmost four images). On all the four FOVs, with increasing R_d/R_s, the intensities at bright regions seen at R_d/R_s of 5/95 became weaker, and the differences between the dark and bright regions decrease. That is, the peak intensity is stronger when the reflectance is specular dominant, while the brightness has better uniformity when diffuse reflectance increases.

Figure 7(a) summarizes the peak radiance for the four different FOVs shown in Fig. 6 at different R_d/R_s. The peak radiance basically decreases with R_d/R_s. The peak radiance at $R_d/R_s = 75/25$ was less than half of those at $R_d/R_s = 5/95$ except for G1♯17U, where the image has good uniformity. Only at G1♯17U receiver, the intensity increased with increasing R_d/R_s from 50/50 to 75/25. Excluding those special cases, the peak radiance decreases with increasing the diffuse reflectance.

In Fig. 7(b), the same plot was made for averaged radiance. The averaged values increased on GA♯17, G1♯17U, and G1♯17D with R_d/R_s. On the other hand, it decreases on G1♯17R with increasing R_d/R_s.

IV. DISCUSSION

A. Required integration time

Here, based on the calculations shown in the previous section, we discuss the feasibility of the diagnostic system as calculating signal and noise levels. In Table II, parameters used for the calculation of expected signal and noise levels are shown. Using the calculated radiance and the information of the detector in Table II, we can assess the signal intensity (number of photons) at the detector and compare to the noise. The transmissions of optics and laser are in the ranges of 3-4.3 and 1.8-3%, respectively. The specific detectivity of 2.5×10^{12} cm$\sqrt{\text{Hz}}$/W is assumed to calculate the noise equivalent power. The detector size is 8×8 μm^2, and the aperture diameter of GA is roughly four times greater than those of G1. We assumed the exposure time of 1 s and added readout noise as considering the number of iteration. Even if the image is very noisy with the SNR of less than unity, the quality of image can be improved by increasing the iteration such as the method used in ghost imaging[7]. We chose four FOVs in ♯17 similar to Sec III B. The SNR levels will be similar to other sections if the direction of the detectors is the same, as was discussed in Sec. III A.

Figure 8(a-d) shows profiles of required integration time, t_i, to achieve the SNR of three, which is thought to be the minimum value to obtain useful signals, on GA♯17, G1♯17U, G1♯17R, and G1♯17D, respectively. On G1♯17U and G1♯17R receivers, t_i is less than 1 min. It is likely that images can be taken for those FOVs with enough quality. The image quality will be improved if the surface is diffusive on G1♯17U. Concerning GA, a long integration time will be required around the divertor plates, where signal intensity strongly depends on the diffuse reflection component. Enough quality may be obtained if the divertor tiles become optically diffusive. Unfortunately, it is likely that signal level will not be enough on G1♯17D. The image quality will be slightly improved when the surface is optically diffusive, but it may be insufficient for detailed inspection for several minutes of time. Here, the SNR of three was used for assessment; it may be necessary to increase it to $\sim$10 for higher

quality images sometimes. It requires to increase the integrating time by roughly an order of magnitude from the case of the SNR of three, because the SNR is improved with a square root of the integration time.

If divertor views are inevitable, one option is to take longer time for integration like an hour or so for lower facing receivers. In the next subsection, we will discuss about possible way to shorten the total integration time as optimizing the exposure sequence. Other option may be an introduction of LIDAR. Images can be taken by irradiating pulsed lasers to the facing wall and scanning the position while the reflected signal is captured by a single detector. Although this system will require slightly complicated optics, it has an advantage that the images at different ports can be taken at the same time, while the above illumination option requires sequential procedure for different receivers. Further feasibility study is required for the LIDAR option; the issue is beyond the scope of this paper and will be discussed elsewhere in future.

B. Concurrent integration

As was discussed up to now, it is likely that five GA receiver and four down-facing receivers on G1 will require hour-long exposure time. It would be fine for other 11 receivers to take images sequentially, because each exposure time should be a minute or two. However, it would be nine hours for GA receivers and down-facing receivers if images were taken sequentially for an hour for each. Thus, it would be beneficial to seek a way to shorten the time to take all the images concurrently. In Sec. III A, it was revealed that the major contributions are from less than 10 sources. Thus, it may be possible to take the images together at the same time. Here, for a simple case study, we assumed that images are taken at the same time for all the five GA receivers. That is, all the five GA sources should be turned off when taking images of GA receivers. In the same manner, we also assumed that four down-facing receivers are recorded at same time, though it requires turning off all the down-facing receivers while recording. It is noted that because GA sources are major contributor for some down-facing receivers and vice versa, it is not likely a good idea to take images together at GA and G1 down-facing receivers at the same time.

In Fig. 9, the reduction ratios of the signals in the sequentially recording cases to the concurrent recording cases are shown. Two different reflection cases with $R_d/R_s = 5/95$ and 50/50 were investigated. For GA receivers, the reduction ratios increased with increasing the diffuse reflectance, but they were less than 10%; the impact of concurrent recording would be minor. Concerning the G1 down-facing receivers, the reduction ratio decreased with increasing the diffuse reflectance. The receiver at ♯9 will have ≈30% reduction, but the reduction ratios are less than 15% for the other three receivers and will be fine.

Thus, basically, concurrent recording will work, and it will shorten the total integration time by a factor of 4-5. If the intensity of G1♯9D receiver is not enough, we can record images on G1♯9D while taking images at GA receivers as well, because G1♯9D will not be a major contributor to GA receivers, as shown in Table I.

V. CONCLUSIONS

Ray tracing simulations were conducted for feasibility study of ITER in-vessel lighting system by using the existing (IR) and visible wide-angle viewing systems. There are five field of views (FOVs) from upper port and 15 FOVs from equatorial ports. For FOVs on equatorial ports, some sources directly irradiated right and left-facing receivers and formed a bright spot, which easily leads to saturations of detectors. Therefore, selection of the sources is necessary not to form the bright spot on detectors. Moreover, it was also shown that more than 90% of the contribution was from less than major 10 sources for each receiver, though there are potentially 19 sources. Because 5-10 major sources will decide most of the radiance, only using major sources will be an option for recording.

Optical reflectance of wall is one of the major input parameters for the simulation, and we used combination of diffuse to specular reflections. When increasing the ratio of diffuse to specular reflectance, R_d/R_d, strong peaks decreased, and uniformity of the radiance improved. Most of the cases, except for side-facing receivers, the averaged radiance increased with increasing R_d/R_s. Thus, it is likely that diffusive wall is more beneficial for the lighting system.

We assessed the required integration time as calculating the signal and noise levels for typical FOVs: GA and G1 receivers facing upward, sides, and downward. It was found that a minute of integration will be sufficient to obtain enough quality images for receivers facing upward or sides on G1. On GA receivers, the intensity around the divertor is strongly depends on the reflectance property. If the wall is specular, it takes much longer than minutes to take high quality images, while couple of minutes is likely enough to take images when $R_d/R_s = 50/50$. On the other hand, on the downward receivers, it may take hours to obtain high quality images. To shorten the total integration time, we can sum up some receivers and record images together. For example, GA receivers do not contribute each other so much, it is possible to record all the GA receivers together. In a similar manner, G1 down-facing receivers can be recorded concurrently. This will help shortening the total inspection time. If the integration time is still too long, one of the other options is an introduction of LIDAR method. The feasibility of the LIDAR technique is planned and will be conducted in near future.

ACKNOWLEDGMENTS

One of the authors (S.K.) thanks Prof. M. Aramaki of Nihon University for useful comments about signal to noise ratio assessment. This work was supported in part by a Fund for the Promotion of Joint International Research 17KK0132 from the Japan Society for the Promotion of Science (JSPS).

The views and opinions expressed herein do not necessarily reflect those of the ITER Organization.

REFERENCE

[1]R. Reichle *et al.*: Review of Scientific Instruments **83** (2012) 10E520.
[2]S. Vives, M. Aumeunier, C. Guillon, L. Letellier, L. Doceul, M. Proust, C. Portafaix, T. Loarer, N. Lapcevic, N. Lefevre, M. Moll, M. Medrano, V. Martin, F. L. Guern and J. Piqueras: Fusion Engineering and Design **146** (2019) 2442 , sI:SOFT-30.
[3]M.-H. Aumeunier and J.-M. Travere: Review of Scientific Instruments **81** (2010) 10E524.
[4]S. Kajita, M. D. Bock, M. von Hellermann, A. Kukushkin and R. Barnsley: Plasma Physics and Controlled Fusion **57** (2015) 045009.
[5]S. Kajita, E. Veshchev, S. Lisgo, R. Reichle, R. Barnsley, M. Walsh, A. Alekseev, A. Gorshkov, D. Vukolov, J. Stuber and S. Woodruff: Plasma Physics and Controlled Fusion **55** (2013) 085020.
[6]S. Kajita, E. Veshchev, S. Lisgo, R. Barnsley, P. Morgan, M. Walsh, H. Ogawa, T. Sugie and K. Itami: Journal of Nuclear Materials **463** (2015) 936.
[7]B. Sun, M. P. Edgar, R. Bowman, L. E. Vittert, S. Welsh, A. Bowman and M. J. Padgett: Science **340** (2013) 844.

TABLE I. A summary of the sources formed bright spots, the main sources contributing to the total radiance profile, and their fractions.

FOV	Bright spot source	Major source	Contribution
GA♯2	–	G1♯9L	47.7%
GA♯8	–	G1♯12D	66.8%
GA♯11	–	G1♯3L	33.6%
GA♯14	–	G1♯3L	44.4%
GA♯17	–	G1♯3D	56.5%
G1♯3U	–	G1♯3D	22.1%
G1♯3R	G1♯9L	G1♯12L	68.0%
G1♯3L	G1♯17R	G1♯12R	44.4%
G1♯3D	–	GA♯17	58.0%
G1♯9U	–	G1♯9D	22.5%
G1♯9R	G1♯12L	G1♯17L	57.7%
G1♯9L	G1♯3R	G1♯17R	53.6%
G1♯9D	–	G1♯12D	31.1%
G1♯12R	G1♯17L	G1♯3L	67.5%
G1♯12L	G1♯9R	G1♯3R	51.0%
G1♯12D	–	GA♯8	63.0%
G1♯17U	–	G1♯17D	23.2%
G1♯17R	G1♯3L	G1♯9L	54.9%
G1♯17L	G1♯12R	G1♯9R	64.9%
G1♯17D	–	GA♯14	34.7%

TABLE II. Parameters used for the calculation of expected signal and noise levels.

Parameter name	Value
Optics transmission	3-4.3%
Laser transmission	1.8-3%
Specific detectivity	2.5×10^{12} cm$\sqrt{\text{Hz}}$/W
Detector size	8×8 μm^2
Aperture diameter (GA)	18 mm
Aperture diameter (G1)	4-4.6 mm
Readout noise	22 electrons

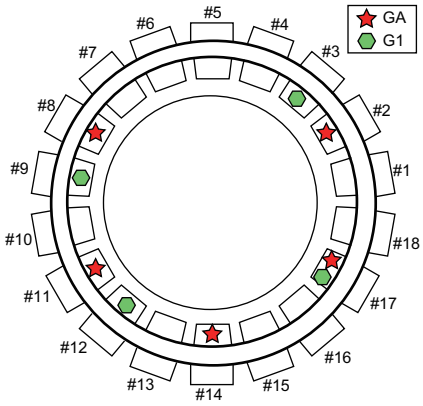

FIG. 1. A schematic of ITER from top with port number. Red star and green hexagonal markers correspond to the ports used for 55.GA and 55.G1, respectively.

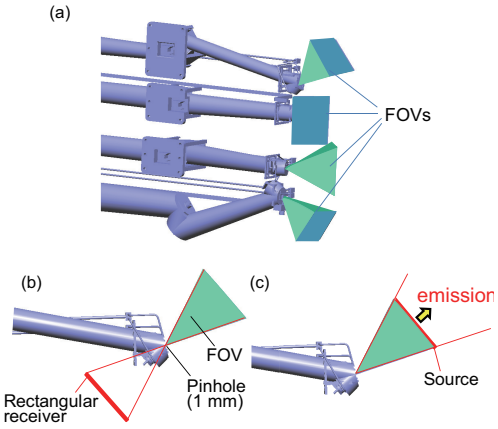

FIG. 2. (a) A computer aided design diagram of one of the 55.G1 system including FOVs, and (b,c) schematics representing the configurations of the receiver and the source, respectively.

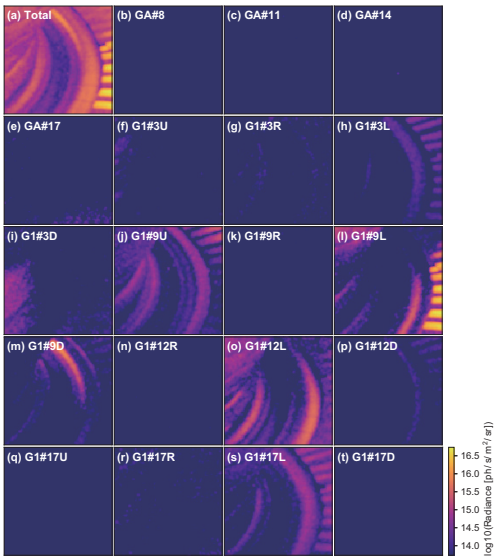

FIG. 3. (a) Total radiance profile of GA♯2 receiver and (b-t) radiance profiles from 19 sources, respectively. The power of each source was assumed to be 1 W. The ratio R_d/R_s was assumed to be 5/95.

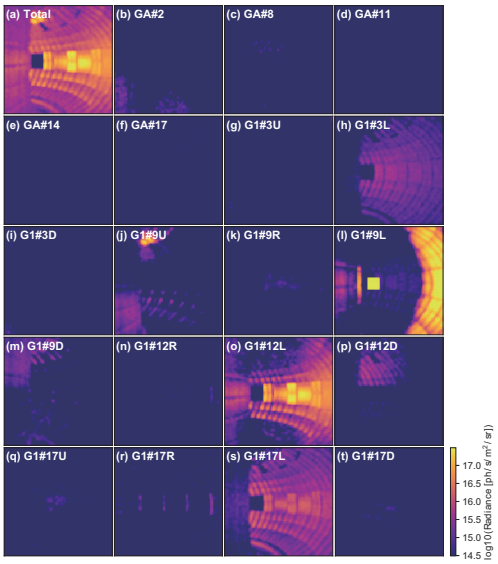

FIG. 4. (a) Total radiance profile of G1♯3R receiver and (b-t) radiance profiles from 19 sources, respectively. The power of each source was assumed to be 1 W. The ratio R_d/R_s was assumed to be 5/95.

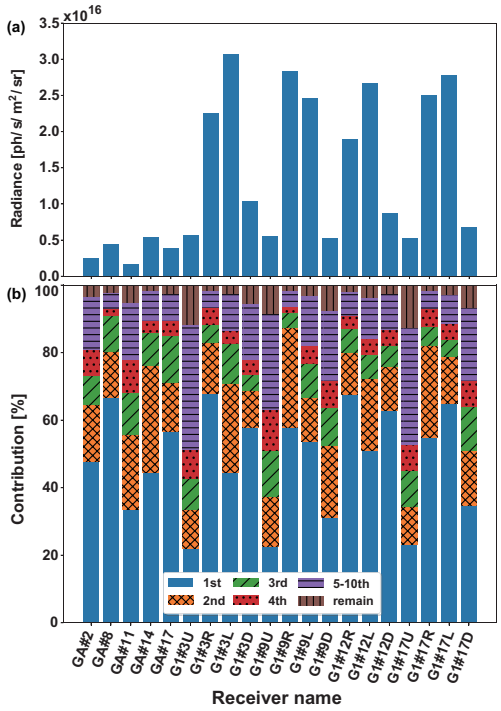

FIG. 5. (a) The averaged radiances on the 20 receivers and (b) fractions of the contribution from major sources to the averaged radiance.

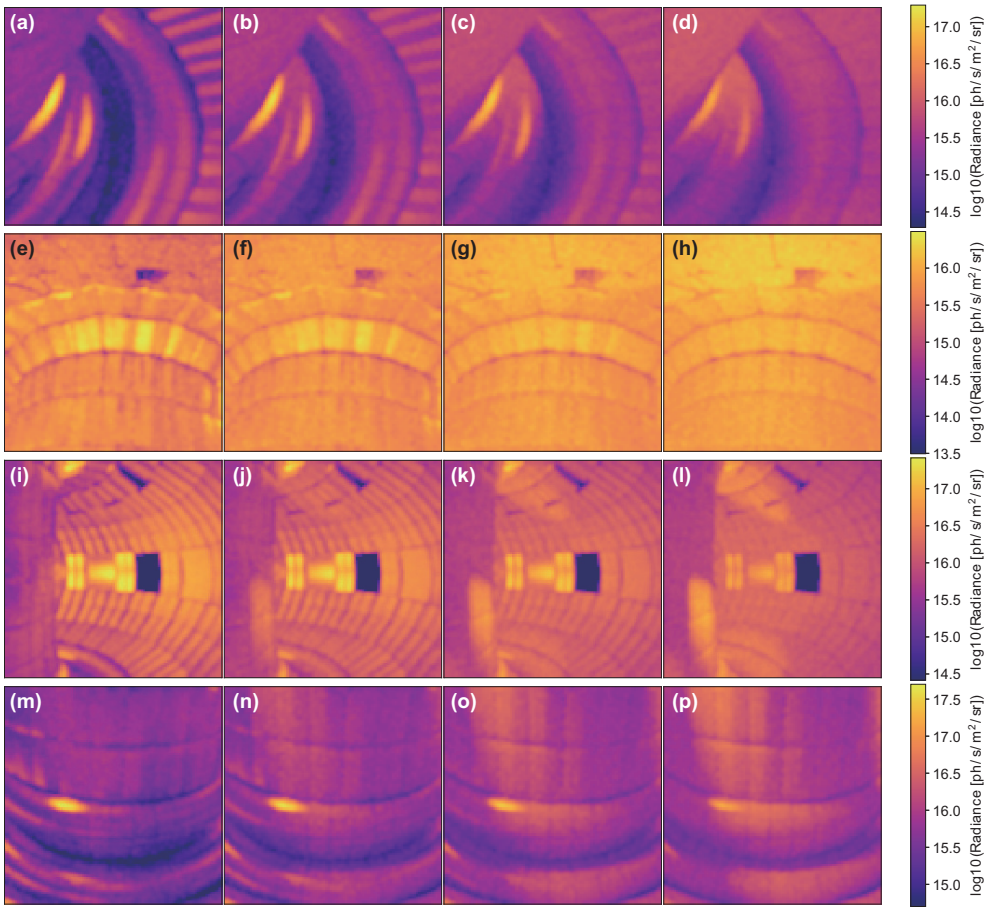

FIG. 6. Radiance profiles of typical four receivers ((a-d)GA♯17, (e-h)G1♯17U, (i-l)G1♯17R, and (m-p) G1♯17D) at different R_d/R_s. The ratio R_d/R_s is (a,e,i,m) 5/95, (b,f,j,n) 25/75, (c,g,k,o) 50/50, and (d,h,l,p) 75/25.

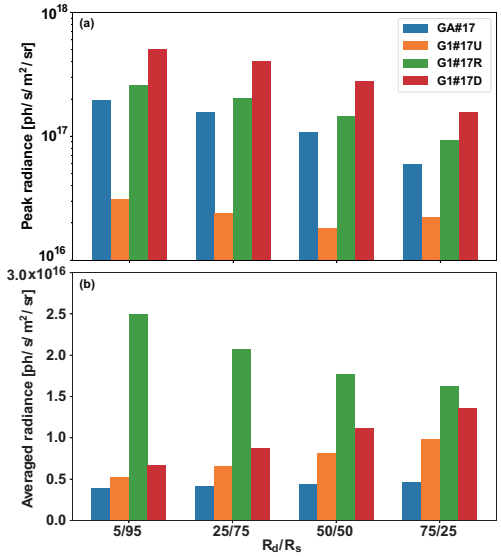

FIG. 7. Summary of (a) the peak radiance and (b) averaged radiance for the four different FOVs shown in Fig. 6 at different R_d/R_s.

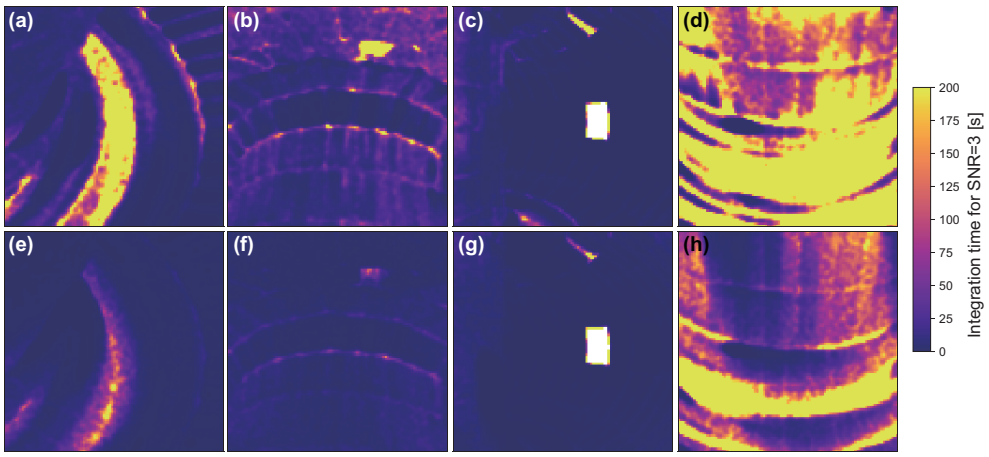

FIG. 8. Profiles of required integration time to achieve the signal to noise ratio of three. (a-d) and (e-h) corresponds to the cases with R_d/R_s of 5/95 and 50/50, respectively. Field of views are as follows: (a,e) GA♯17, (b,f) G1♯17U, (c,g) G1♯17R, and (d,h) G1♯17D.

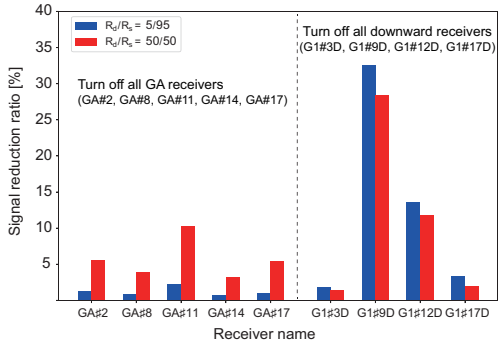

FIG. 9. The signal reduction ratios from the sequentially recording cases to the concurrent recording cases. Two different reflection cases with $R_d/R_s = 5/95$ and 50/50 are shown.